RSC Advances

PAPER

View Article Online
View Journal | View Issue

Cite this: *RSC Adv.*, 2025, **15**, 28285

Low-energy carbon ion irradiation-induced phase evolution in thermally treated Ni/Si bilayers

Khushboo Shah,[a] Ratnesh Pandey,[a] Devarani Devi,[b] Sunil Ojha,[b] Mukul Gupta,[c] Gurupada Maity,[d] Sanjeev Kumar[e] and Santosh Dubey *[a]

Received 12th June 2025
Accepted 1st August 2025

DOI: 10.1039/d5ra04171f

rsc.li/rsc-advances

In this paper, we report the effect of low-energy carbon ion irradiation on the thermally annealed nickel–silicon bilayer samples. The primary objective is to analyse and interpret the formation of various nickel silicide phases, their evolution, and stability under ion irradiation. The bilayer samples were fabricated using magnetron sputtering at room temperature, with a 100 nm nickel top layer and a 100 nm silicon buffer layer deposited on a silicon substrate. The deposition was carried out under a base pressure of 7.02×10^{-7} mbar and a gas pressure of 4.14×10^{-3} mbar. These samples were then annealed at 500 °C for one hour in an argon atmosphere to nucleate various nickel–silicide phases. Ion irradiation was carried out using carbon ions of energy 120 keV for two different fluences 3×10^{15} and 1×10^{16} ions per cm^2. Grazing Incidence X-Ray Diffraction (GIXRD), Transmission Electron Microscopy (TEM), and Rutherford Backscattering Spectroscopy (RBS) techniques were employed to characterize the resulting phases in the thin films. The findings indicate that low-energy irradiation of pre-annealed and unannealed Ni/Si bilayer samples results in significant structural modifications, which are further confirmed by TEM analysis.

1. Introduction

Metal silicides play an important role in modern technology, finding applications in microelectronics,[1–6] protective coatings,[7–9] and optoelectronic devices.[10,11] Among various materials for similar applications, such as cobalt silicide and tungsten silicide, nickel silicides have garnered significant interest.[12–16] Extensive research has been conducted on nickel film deposition over silicon substrates, followed by thermal treatment to induce phase formation.[17–19] Nickel and silicon form a diffusion couple,[20] in which interdiffusion of Ni and Si across the interface results in nucleation of various silicide phases at different annealing conditions. Interdiffusion of Ni and Si is also possible *via* ion irradiation. Therefore, investigating the structural changes in Ni–Si thin films under both thermal processing and ion irradiation may open novel pathways for understanding phase formation and stability, and interfacial evolution in such systems.[21]

Ion beam irradiation has been successfully employed as a tool to synthesize new materials, modify intrinsic properties of existing materials, initiate phase transformations, introduce damage or defects at the atomic level, to study the extreme effects of radiation environment on a given material,[22,23] *etc.* Recently, 1 MeV Si+ ions were used to nucleate NiSi phases in bilayer Si (~5 nm)/Ni (~15 nm)/Si thin films at room temperature.[24] In another investigation, 120 keV Si ions were used on Ni (~30 nm)/Si and Ni (~60 nm)/Si monolayer thin films to nucleate different orientations of NiSi phases at room temperature.[26] The crystallinity of NiSi phases was observed to depend on the thickness of the Ni layer: NiSi crystallinity was found to be better in a 60 nm Ni layer thickness as compared to a 30 nm Ni layer thickness.[26] The characteristics of ions employed in these experiments (*e.g.*, charge state, size, atomic mass, *etc.*) seem to play an important role in the formation of nickel silicide phases. When light ions are used, a non-uniform silicide growth was observed, while heavy ions are observed to result in uniform silicide formation.[25,26]

Thermal annealing has frequently been used to synthesize silicides in nickel film deposited on a silicon substrate.[13,27,28] The effect of thermal treatment on nickel silicides phases[29–31] has also been studied in-depth in numerous experiments, and its application in many domains has also been explored.[7,15,16,32,33] In all these investigations, a typical sequence of silicide formation has been observed: Ni_2Si forms at temperatures below 300 °C, NiSi appears between 300–700 °C (being the phase with the lowest electrical resistance), and $NiSi_2$ starts forming above 700 °C. However, when the deposited film thickness is less than 5 nm, this phase sequence is altered due to changes in the kinetics and dynamics of silicide formation.

[a]*Department of Physics, School of Advanced Engineering, UPES, Dehradun, 248001, India. E-mail: santosh.dubey@ddn.upes.ac.in*
[b]*Inter University Accelerator Centre (IUAC), Vasant Kunj, Delhi, 110067, India*
[c]*UGC-DAE Consortium for Scientific Research, Indore, 452017, India*
[d]*Department of Physics, School of Basic Sciences, Galgotias University, 203201, India*
[e]*Department of Chemistry, School of Advanced Engineering, UPES, Dehradun, 248001, India*

This highlights the critical role of film thickness in the nickel silicide formation process.[34,35] In one such investigation, nickel silicide phase formation was studied using a rapid thermal annealing process (RTP) in samples with varying nickel layer thickness. It was observed that the sample with a thinner Ni layer tends to form a uniform silicide phase readily than a thicker layer, which possibly leads to incomplete phase transition or multiple phase formation.[40,41]

In the present experimental investigation, the primary objective is to examine the effect of low-energy ion beam irradiation and thermal annealing on the formation of nickel silicide phases. To assess the impact of irradiation on the structural evolution of the bilayer, both annealed and unannealed samples were exposed to low-energy negative ion irradiation. This approach allows for a comparative study of how ion irradiation influences the phases formed in annealed and unannealed samples. Thermal annealing is done at 500 °C for 1 h in an argon atmosphere. At this temperature, an appreciable number of nickel monosilicide (NiSi) phases is observed to form and grow with significant crystallinity. Along with the NiSi phase, other phases like Ni_2Si, SiO_2 are also observed. The findings from this study will provide valuable insights into the role of irradiation in modifying interfacial reactions and phase evolution in bilayer thin film systems.

2. Materials and methods

Nickel–silicon bilayer film was deposited using magnetron sputtering[36] under high vacuum conditions (10^{-7} mbar) at room temperature (RT), minimizing the contamination. With the presence of argon gas (for plasma) and an RF power of 40 W for both nickel and silicon, the deposition rates are set to 36 Å min^{-1} for nickel and 25.2 Å min^{-1} for silicon, in order to deposit 100 nm of each film. The substrate was cleaned under the standard procedure before the deposition. The samples were cut into pieces of 1 cm × 1 cm. The resulting deposition consisted of a 100 nm nickel layer and a 100 nm silicon layer on a silicon substrate [c-Si(111)]. Following deposition, some of the samples were annealed at 500 °C for 1 hour in an argon atmosphere with a temperature ramp of 20 °C min^{-1} during heating, followed by natural cooling, in a tubular furnace. The sample deposited at RT is named as S1, and the sample annealed at 500 °C for 1 hour is named as S2.

The sample details is collectively summarised in the tabular form given in Table 1.

Both S1 and S2 samples were subjected to low-energy negative ion beam irradiation (using carbon ions) in the Negative Ion Implanter beam Facility (NIIBF, IUAC, New Delhi) with 120 keV carbon ions at room temperature under a high vacuum of 5×10^{-6} torr, at 3×10^{15} and 1×10^{16} ions per cm^2 fluences.

Detailed crystallographic information about the growth and evolution of phases in the pristine and irradiated samples was obtained by Grazing Incidence X-ray Diffraction (GIXRD) measurements with Cu-Kα radiation (λ = 1.54 Å), at room temperature, using a PANalytical model EMPYREAN X-ray diffractometer. The Diffractogram was recorded at an incidence angle of 0.5°, in the angular region (2θ) ranging from 20° to 80° and at a scan rate of 0.05° s^{-1}. Rutherford backscattering spectrometry (RBS) was employed to evaluate elemental composition and depth profiling of pristine and irradiated samples, using 2 MeV He-ions, from 1.7 MV Tandem Pelletron (IUAC, New Delhi). The beam was incident at an angle (θ) of 3°, facilitating high-resolution depth profiling for intricate compositional analysis.

Further, the pristine and irradiated S2 sample (at 3×10^{15} ions per cm^2) were subjected to high-resolution transmission electron microscopy (HRTEM) at the user facility TEM Lab of IUAC, Delhi. Planar TEM samples were prepared with the powder method using ultra ultra-sonicator, where the thin film is set in IP liquid and is sonicated for 10 minutes at the working frequency of the sonicator, which is 40 Hz. After this procedure, the liquid that contains fine films of the deposition is drop-cast onto a 300-mesh carbon grid of 3 mm diameter. For HRTEM measurements, a JEOL JEM-F200 High-Resolution Transmission Electron Microscope equipped with a Thermal Field Emission Electron Gun (TFEG) was utilized. All measurements were conducted at an accelerating voltage of 200 kV. TEM imaging, along with Selected Area Electron Diffraction (SAED) techniques, were employed to investigate the structural modifications induced by irradiation. These techniques offered detailed and comprehensive information regarding the structural, compositional, and crystallographic alterations resulting from the irradiation.

3. Results and discussion

3.1 GIXRD diffractogram

Fig. 1 shows the GIXRD pattern of the S1 and S2 samples. The 2θ value obtained from the experimental data was compared with that of the standard value from the material project,[37] an open-access database. In the as-deposited sample S1, peaks corresponding to Ni(111) at 44.69°, NiSi(103) at 52.13°, and NiSi(203) at 76.56° are observed. While in the annealed sample S2, additional peaks in the GIXRD pattern were observed, indicating the formation of new phases including Ni_2Si (120) at 43.54° and different orientations of NiSi like (103), (032), (041) and (203) at 52.20°, 63.18°, 75.68° and 76.68° respectively. The

Table 1 Sample description and deposition details

Sample	Element	Thickness, Å	Power voltage (watt)	Deposition rate, Å min^{-1}
Bi-layer nickel on top	Nickel	1000	40	36
	Silicon	1000	40	25.2

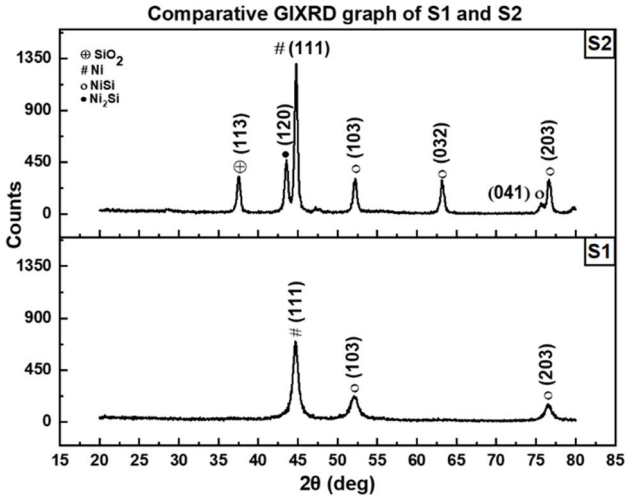

Fig. 1 XRD patterns of Ni/Si bilayer, S1 and S2 showing nickel silicide phase formation of and residual Ni after annealing.

common phases in both samples are Ni(111), NiSi(103) and NiSi(203). The crystallite sizes corresponding to these phases have been listed in Table 2. Debye–Scherrer equation,[38] given by $D = \frac{k\lambda}{\beta \cos \theta}$, was used to calculate the crystallite size of the phases formed. Here, k is the Debye–Scherrer constant, usually taken as 0.9,[39] λ is the wavelength of the Cu-K_α (1.54 Å), β is the FWHM value and θ is the half value of Bragg's angle.

The crystallite sizes of all three phases increase significantly upon annealing. This suggests improved crystallinity during thermal treatment.[40,41] Moreover, the emergence of additional NiSi and Ni_2Si phases after annealing implies growing crystallinity and confirms interdiffusion and solid-state reactions between the layers.[42–44]

To examine the impact of low-energy ion irradiation, both types of samples, S1 and S2, were irradiated using carbon ions with an energy of 120 keV for two different fluences 3×10^{15} ions per cm^2 and 1×10^{16} ions per cm^2. The GIXRD pattern of the pristine and irradiated S1 sample is shown in Fig. 2(a), and the effect of irradiation on the peak positions, FWHM, and crystallite sizes has been displayed in Table 4, with corresponding variation in crystallite size in Fig. 2(b).

It can be seen that with increasing fluence, a gradual increase in the crystallite size D is observed. The angle of diffraction is observed to increase slightly at 3×10^{15} ions per cm^2 indicating compressive strain in the lattice. Angle of diffraction seems to decrease as flux is increased further (at 1×10^{16} ions per cm^2) due to lattice relaxation. This variation has been displayed in Fig. 2(a) and Table 4.

The observed growth in crystallite size with ion fluence can be effectively described by a power-law relation[45,46] of the form $D^n - {D_0}^n = K\varphi$,[47–49] where D is the crystallite size (after irradiation), D_0 is the initial crystallite size (unirradiated), φ is the ion fluence, K is a material-specific growth constant, and n is the growth exponent which generally ranging between 2 and 4 for diffusion-driven mechanisms triggered by thermal annealing or ion irradiation. This trend is attributed to transient thermal spikes produced during collision cascades, which locally elevates the temperature and promote atomic mobility.[46,50] Simultaneously, radiation-enhanced diffusion facilitated by the formation of vacancies, interstitials, and other point defects further supports crystallite coalescence and reordering.

The growth constant K is calculated using $K = \frac{D^2 - {D_0}^2}{\phi}$ and indicates the efficiency of crystallite growth and varies across different phases depending on their atomic packing structure and defect tolerance.[51,52] K is calculated for the phases Ni(111), NiSi(103), and NiSi(203), assuming diffusion-governed growth with $n = 2$.[53] Table 3 illustrates the calculated growth constant and highlights the crystallite evolution. The difference in crystallite size is evaluated by using the crystallite size of the as-deposited or unirradiated sample as D_0, and the final crystallite size after irradiation as D. Thus, due to its closely packed FCC structure, the Ni(111) phase exhibits a higher K value (as confirmed by the calculations), indicating efficient energy dissipation and sustained grain coarsening[49,54] at elevated fluences. In contrast, the NiSi(103) phase, a high-index orthorhombic plane with a more open structure, shows a decreasing trend in K, suggesting stronger defect trapping and reduced atomic diffusion. Meanwhile, the NiSi(203) phase, although also a high-index and loosely packed structure, shows a slight increase in K with an increase in fluence, potentially due to its irradiation-driven structural stability and reordering of preferential orientation. However, the increase in K for this phase remains subtle and not significantly pronounced.

On the other hand, the S2 film displays a different behaviour under ion irradiation, as shown in the GIXRD pattern of pristine and irradiated S2 samples in Fig. 3. Before performing irradiation, S2 film was annealed at 500 °C, which resulted in the formation of various phases like Ni_2Si(120), NiSi(103), NiSi(032), NiSi(041), NiSi(023), in addition to Ni(111) and SiO_2(113) (see Fig. 3). Thereafter, the annealed S2 film was irradiated with carbon ions having an energy of 120 keV at different fluences 3×10^{15} ions per cm^2 and 1×10^{16} ions per cm^2. The GIXRD pattern shows a significant reduction in the intensity of all the peaks as fluence increases, signifying irradiation-induced amorphization.[55]

Table 5 contains the crystallite sizes of various phases at different fluences and their peak positions in the diffractogram. The crystallite sizes for different phases were calculated using

Table 2 Comparison of the crystallite size (D) for phases Ni(111), NiSi(103), and NiSi(203), indicating significant grain growth post-annealing

Sample type	2θ (deg.)	Phase (orientation)	D (Å)
S1	44.69	Ni(111)	85.77
	52.13	NiSi(103)	65.48
	76.56	NiSi(203)	68.35
S2	44.76	Ni(111)	189.12
	52.2	NiSi(103)	143.72
	76.67	NiSi(203)	177.32

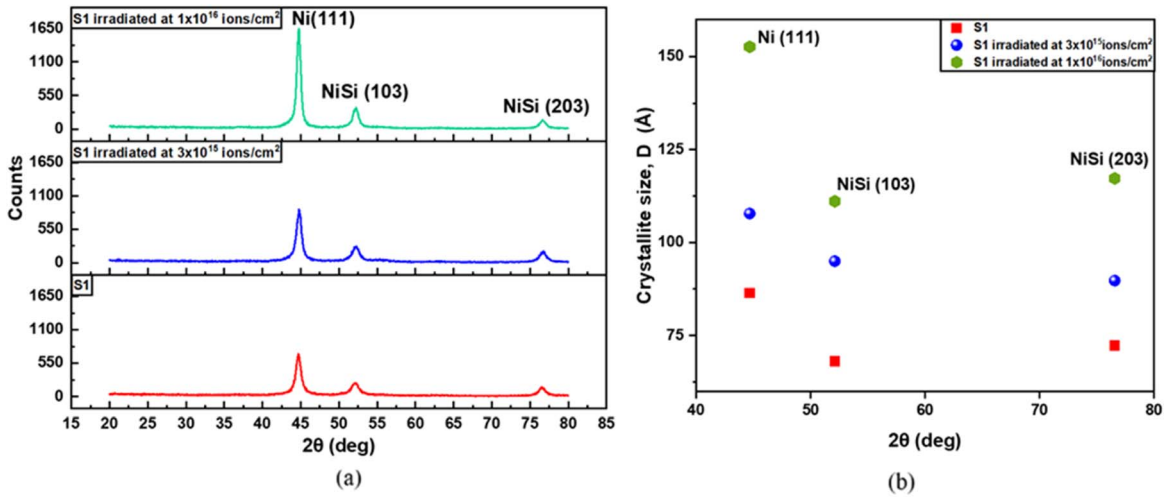

Fig. 2 (a) GIXRD patterns of unannealed samples under different irradiation conditions. The XRD patterns compare the crystallographic changes in an un-annealed samples subjected to different ion fluences, (b) crystallite size variation of Ni(111), NiSi(103) and (203), at different irradiation fluence.

Table 3 Table for calculated growth constant (K) for distinct Ni(111), NiSi(103), and NiSi(203) phases following ion irradiation at fluences of 3×10^{15} and 1×10^{16} ions per cm^2. The data illustrate phase-dependent growth dynamics and highlight the crystallite evolution

Phase	D_0 (initial crystallite size) un-irradiated (nm)	Irradiation fluence (ions per cm^2) (φ)	D (final crystallite size) irradiated (nm)	$D^2 - {D_0}^2$ (nm^2)	K (growth constant)
Ni (111)	8.65	3×10^{15}	9.14	8.717	2.91×10^{-15}
		1×10^{16}	12.27	75.73	7.57×10^{-15}
NiSi (103)	6.81	3×10^{15}	7.86	15.40	5.14×10^{-15}
		1×10^{16}	8.11	19.39	1.94×10^{-15}
NiSi (203)	7.23	3×10^{15}	7.34	1.60	5.08×10^{-16}
		1×10^{16}	8.73	23.94	2.39×10^{-15}

the Debye–Scherrer[39] formula. From Table 5, we see that the crystallite size of Ni_2Si (120) and NiSi (103) increase when the sample is irradiated with a fluence of 3×10^{15} ions per cm^2, whereas for the other phases, we see a decrease in the crystallite size. In Fig. 3, the intensity of all the peaks is observed to decrease. In Ni_2Si (120) and NiSi (103) phases, a decrease in the intensity of the peaks under irradiation shows amorphization of most of the crystallites of these orientations, except for a few. However, the increase in the crystallite size of the remaining crystallites of these orientations may be due to localized recombination of vacancy and interstitials (Ni–Ni, Si–Si or Ni–Si interstials in dumbbell configurations)[56] transported there by radiation-enhanced diffusion. A decrease in the crystallite size of the remaining phases might be due to irradiation-induced amorphization.[55]

The phase-specific tolerance to irradiation is principally governed by key factors that influence radiation resistance: (a) atomic density, (b) bonding energy, and (c) atomic packing of

Table 4 Crystallite size calculated using Scherrer equation for Ni(111), NiSi(103) and (203), phases in S1 thin films subjected to ion irradiation with fluence 3×10^{15} ions per cm^2 and 1×10^{16} ions per cm^2

Fluence (ions per cm^2)	Peak type	Peak position 2θ (degree)	FWHM, β (degree)	Crystallite size, D (Å)
Unirradiated	Ni(111)	44.67	0.993	86.458
	NiSi(103)	52.1	1.298	68.098
	NiSi(203)	76.56	1.399	72.311
3×10^{15}	Ni(111)	44.76	0.94	91.362
	NiSi(103)	52.21	1.25	78.607
	NiSi(203)	76.66	1.38	73.357
1×10^{16}	Ni(111)	44.73	0.7	122.67
	NiSi(103)	52.17	1.09	81.117
	NiSi(203)	76.66	1.16	87.269

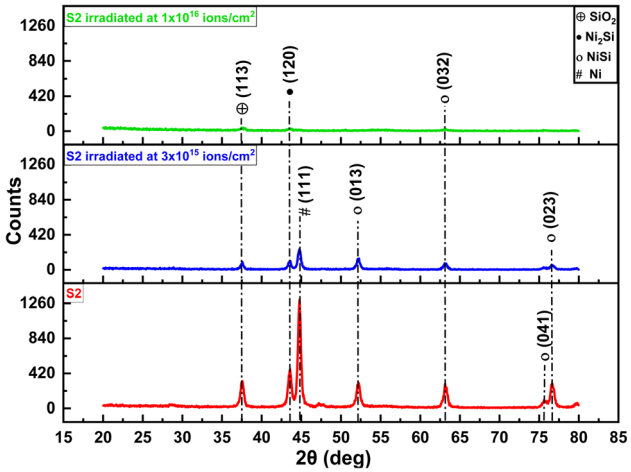

Fig. 3 The GIXRD diffractogram in the figure shows the phases of nickel silicides Ni_2Si and NiSi of different orientation in the annealed sample and samples irradiated post annealing under fluence 3×10^{15} ions per cm^2 1×10^{16} ions per cm^2. The decrease in peak intensities of the phases is clearly visible as the fluence increases indicating progressive amorphization of these silicide phases.

the respective phases.[57–59] Additionally, irradiation along different crystallographic orientations encounters varying planar atomic densities and channel widths. Planes with higher atomic density present greater resistance to defect cascades initiated by ion fluence, acting as barriers, while low-density planes facilitate deeper penetration of defects due to wider atomic spacing.

Under 120 keV C^- irradiation, orientations such as Ni_2Si(120) and NiSi(103) retain or even improve their crystallinity. This is attributed to their tightly packed atomic rows and higher threshold displacement energies, which confine collision cascades to smaller regions. Such confinement promotes in-cascade recombination of vacancies and interstitials, effectively healing damage before it accumulates. In contrast, orientations like Ni_2Si(211) and NiSi(203) possess more open channels and lower displacement threshold energies, which allow collision cascades to spread and enable channelling of primary knock-on atoms deeper into the lattice. This extended cascade overlap inhibits efficient dynamic annealing, facilitates the formation of stable defect clusters, and eventually leads to orientation-dependent amorphization in these phases.[60–62]

The Ni_2Si phase oriented along (120) adopts an orthorhombic δ structure[63] with relatively open lattice planes, resulting in pronounced tensile strain upon irradiation.[64] This strain is readily relieved at the coherent interfaces. By contrast, monoclinic NiSi(103) possesses a densely packed atomic framework that promotes texture evolution under irradiation; the (103) planes thus hinder strain relaxation, leading to localized strain build-up and defect clustering. The unusual persistence of NiSi(103) crystallinity likely stems from orientation-selective recrystallization,[65] whereas Ni_2Si(120) amorphizes more uniformly.[24]

From the Table 5, we also observed that the response to the irradiation depends on the orientation of a certain phase. Under irradiation, phases with certain orientations are affected more than others. This may be due to differences in atomic structure and defect tolerance, which dictate how each phase with a specific orientation responds to the irradiation.[66–68] From this observation, we may say that phases of certain orientations may be more susceptible to damage, while others may withstand the effects of irradiation.[69] As the ion fluence increases, the extent of damage also rises. At the highest fluence of 1×10^{16} ions per cm^2 while all other phases disappear, only SiO_2 (113), Ni_2Si (120), and NiSi (032) remain noticeable with very weak intensity.

Phase formation under irradiation is possible only due to the availability of point defects and defect clusters. The residual concentration of point defects remaining after the thermal spike phase tells about the extent of damage in the material. We have performed TRIM simulations to get an estimate of the point defect concentrations using 120 keV carbon ion irradiation with different fluences. The concentration of point defects (vacancy or interstitial) produced using 120 keV carbon ions at the fluence of 3×10^{15} and 1×10^{16} ions per cm^2, as estimated by TRIM simulation, is found to be approx. 2.2×10^{18} and 7.3×10^{18}, respectively. The displacement energies of nickel and silicon were found to be 25 eV and 15 eV, respectively.

Another effective way of estimating the damage induced by irradiation is to calculate the change in area under the graph or the FWHM of the peaks before and after irradiation. This measurement provides the radiation-induced damage[70] w.r.t the change in FWHM, which has been calculated using the equation below.

$$\Delta\mathrm{FWHM} = \frac{\mathrm{FWHM_{Pristine}} - \mathrm{FWHM_{irradiated}}}{\mathrm{FWHM_{Pristine}}} \times 100 \qquad (1)$$

Fig. 4 shows differences in FWHM of different phases of nickel silicide in pristine (annealed but unirradiated) and irradiated samples. If we compare the FWHM of various phases in

Table 5 Crystallite sizes of different phases in S2 film subjected to ion irradiation of fluence 3×10^{15} ions per cm^2 1×10^{16} ions per cm^2

		Crystallite size D (Å)		
Phase (orientation)	Peak position, 2θ (deg)	Annealed film	Annealed & irradiated film at 3×10^{15} ions per cm^2	Annealed & irradiated film at 1×10^{16} ions per cm^2
Ni_2Si(120)	43.55	187.18	192.9	Very small, not possible to calculate
NiSi(103)	52.2	151.78	158.32	
NiSi(032)	63.19	149.4	137.01	
NiSi(203)	76.68	185.2	138.98	

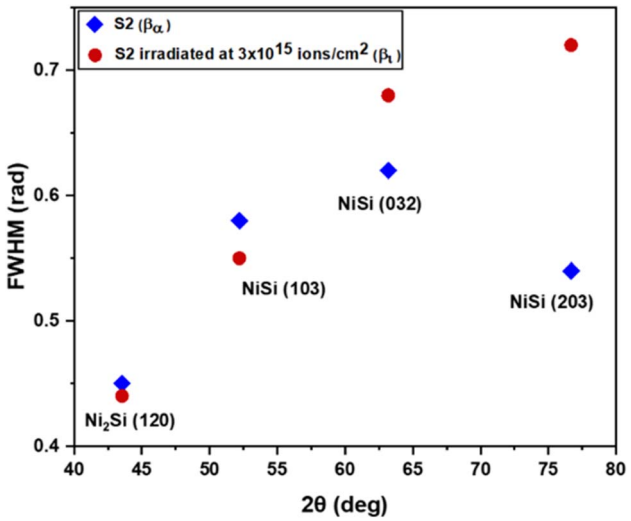

Fig. 4 FWHM comparison of nickel silicide phases; Ni_2Si(120), NiSi(103), NiSi(032) and NiSi(203), in annealed bilayer sample and sample irradiated post annealing.

pristine and irradiated samples, we see that the FWHM is higher for some phases in pristine (Ni_2Si (120) & NiSi (103)) as compared to irradiated samples, whereas for other phases (NiSi(032) and NiSi(203)), the FWHM for irradiated samples is higher than that of pristine.

Under ion irradiation, crystalline materials develop anisotropic strain, evident through variations in peak broadening and corresponding shifts in FWHM across different crystallographic planes.[71] This directional strain originates from non-uniform energy deposition, leading to localized stress fields, defect accumulation, and dislocation loop formation that vary with lattice orientation. These effects are intrinsically governed by factors such as atomic packing density and bond strength anisotropy among the crystallographic directions.[72,73]

Since $D \propto \frac{1}{\mathrm{FWHM}}$, irradiation seems to affect phases of certain orientations more than the others: for instance, the crystallite sizes of NiSi (032) and NiSi (203) are reduced, whereas the crystallite sizes of NiSi (103) and Ni_2Si (120) phases are increased, which we have commented on earlier also. This biased behaviour of irradiation towards phases of different orientations has also been captured using eqn (1), which calculates the percentage of radiation damage (ΔFWHM) of different phases (Table 6). From the table, we see positive and negative values of ΔFWHM, which may be interpreted as below.

ΔFWHM > 0. A positive value of ΔFWHM ($FWHM_{pristine} > FWHM_{irradiated}$) suggests growth in the crystallite size after irradiation compared to the crystallite size in the annealed film (pristine). The growth in the crystallite size might be due to the recombination of irradiation-induced defects (vacancy + dumbbell interstitials) transported *via* radiation-enhanced diffusion. Additionally, a decrease in internal stress during irradiation leads to lower strain-induced broadening. The process can also enhance the orderliness within the crystal structure.[74–76]

ΔFWHM < 0. A negative ΔFWHM ($FWHM_{pristine} < FWHM_{irradiated}$) value indicates radiation-induced amorphization of the phases. This could result from the accumulation of radiation damage in the form of radiation-induced defects such as vacancies, interstitials, *etc.*, or increased lattice strain. In this case, the possibility of recombination is very low, either due to large spatial separation between vacancies and interstitials or due to sustained irradiation, the lattice is not getting enough time for recovery (*via* recombination process).[74–76]

The recombination of irradiation-induced defects is a thermally activated process governed by the availability of mobile point defects and sufficient activation energy[77] for their diffusion. The onset of recombination is highly material-dependent but typically occurs at intermediate temperatures where defects can migrate. Observations of anisotropic strain relaxation or FWHM narrowing upon annealing and irradiation are consistent with such recombination dynamics. Numerous studies[71,78–80] have validated this behavior across metals and semiconductors, making it a universal phenomenon in ion-irradiated materials.

Microstrain in Ni–Si thin films. Microstrain may help us to understand the degree of relaxation or compression in the material due to irradiation-induced or thermal-induced damage. The strain calculation is done for three prominent peaks Ni (111), NiSi (103), and NiSi (203) that appear in all sample types. We have used the following expression to calculate strain:

$$\varepsilon = \left(\frac{\lambda}{D\cos\theta} - \beta\right) \times \frac{1}{\tan\theta} \quad (2)$$

where, λ is the wavelength of the Cu-K_α used in the GIXRD, D is the crystallite size calculated *via* Debye–Scherrer equation, and

Table 6 Impact of ion irradiation on various crystallite phases of Ni–Si thin films (damage calculation)

Scattering angle, 2θ (degree)	Phase (orientation)	FWHM of annealed sample at 500 °C (called pristine)	FWHM of irradiated sample at fluence of 3×10^{15} ions per cm^2	ΔFWHM (%)
37.53	SiO2 (113)	0.55	0.54	2.38
43.54	Ni2Si (120)	0.45	0.44	2.96
44.76	Ni (111)	0.44	0.47	−5.78
52.20	NiSi (103)	0.58	0.55	4.12
63.18	NiSi (032)	0.62	0.68	−9.03
76.68	NiSi (023)	0.54	0.72	−33.25

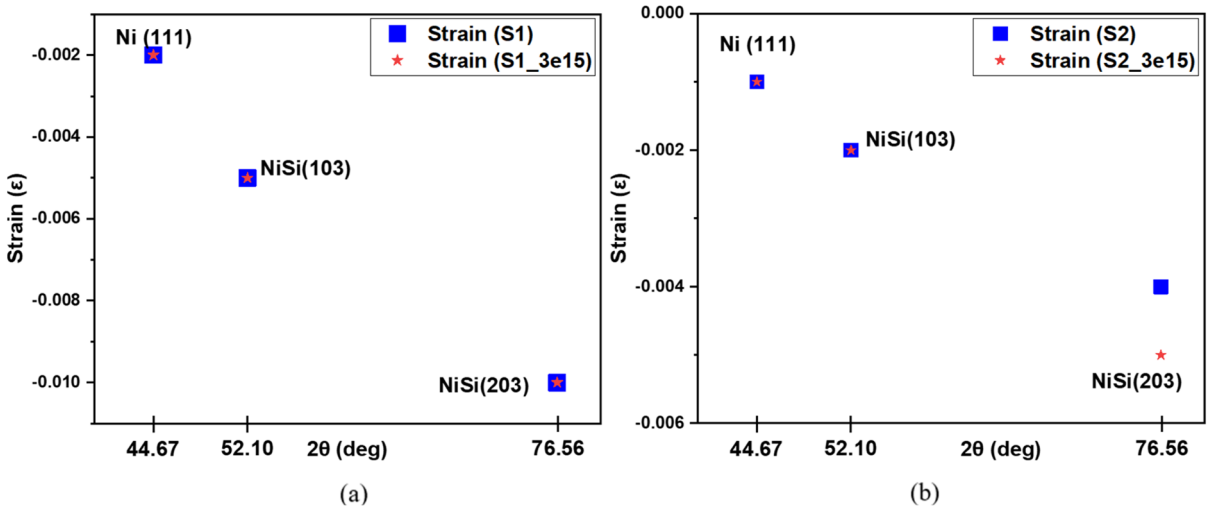

Fig. 5 Strain in (a) as deposited and irradiated samples, and (b) annealed and irradiated post annealing sample in phases Ni (111), NiSi (103) and NiSi (203). The annealing value taken is 3×10^{15} ions per cm^2.

β is the FWHM value, θ is the half value of Braggs angle where the phase is formed.[81] The irradiation fluence considered is 3×10^{15} ions per cm^2. Fig. 5 and Table 7 show that the compressive strain is greater in as-deposited samples (S1) compared to annealed samples (S2). A higher strain in S1 may be due to high interfacial stress as a result of lattice mismatch during deposition (Ni on top of Si layer), which is reduced by annealing. Annealing leads to strain relaxation by allowing atoms to rearrange and settle into lower-energy, equilibrium positions, reducing lattice distortions, and it simply relieves the residual stress built up during deposition. From the figure, we see that the strain value in S2 seems to decrease by more than half from that observed in S1.

During irradiation, there is not much variation in the strain value w.r.t the pristine sample in sample S1. This can be confirmed by comparing the value of S1 & S1_irradiated. A similar inference may be drawn for sample S2 also. However, for the NiSi (203) phase, the strain value seems to increase marginally under irradiation (see Fig. 5 and Table 7). This could be because the irradiation conditions used may be insufficient to relieve or induce lattice strain. Thus, it can be concluded from the values in Table 6, that any observed difference in strain between S1 and S1_irradiated, as well as S2 and S2_irradiated, is residual in nature and not an effect of irradiation. Simply put, thermal treatment is the dominant mechanism for strain relaxation in the studied thin films, while the irradiation conditions employed do not induce measurable structural modifications in terms of lattice strain.

3.2 Rutherford backscattering spectroscopy (RBS)

The Rutherford backscattering method is a non-destructive method which is widely used for the near-surface analysis of elemental composition and depth profiling of solid samples. In this scheme, high-energy proton or He ions is used for the analysis.

Fig. 6 shows the RBS spectra of pristine and irradiated S1 and S2 samples: (a) S1 and S2, (b) S1 and S1_irradiated under 3×10^{15} ions per cm^2 fluence, (c) S2 and S2_irradiated under 3×10^{15} ions per cm^2 fluence. In Fig. 6(a), it is clear from the RBS spectrum that, due to annealing, there is a noticeable alteration in the Ni and Si peaks. The width and height of the Ni peak for S2 is less as compared to those in S1, implying a lower backscattering yield for Ni and Si. Also, interdiffusion between Si and Ni layers can be seen near the interface in the RBS spectrum of the S2 sample. In the RBS spectrum, the peak yield defines the areal density of the element. Therefore, the reduced Ni peak in S2 means a small concentration of Ni on the surface, which seems consistent with the fact that under thermal annealing, Ni atoms diffuse into the Si layer and react there with Si to form silicide phases. The amount by which Ni is reduced on the surface it gets consumed or redistributed to make various nickel

Table 7 Strain values calculated from XRD peak positions for various crystallographic orientations of Ni and NiSi phases in S1 and S2, S1_irradiated and S2_irradiated samples

		Strain			
2θ	Phase (orientation)	S1	S2	S1_irradiated	S2_irradiated
44.67	Ni (111)	−0.002	−0.001	−0.002	−0.001
52.10	NiSi(103)	−0.005	−0.002	−0.005	−0.002
76.56	NiSi(203)	−0.010	−0.004	−0.010	−0.005

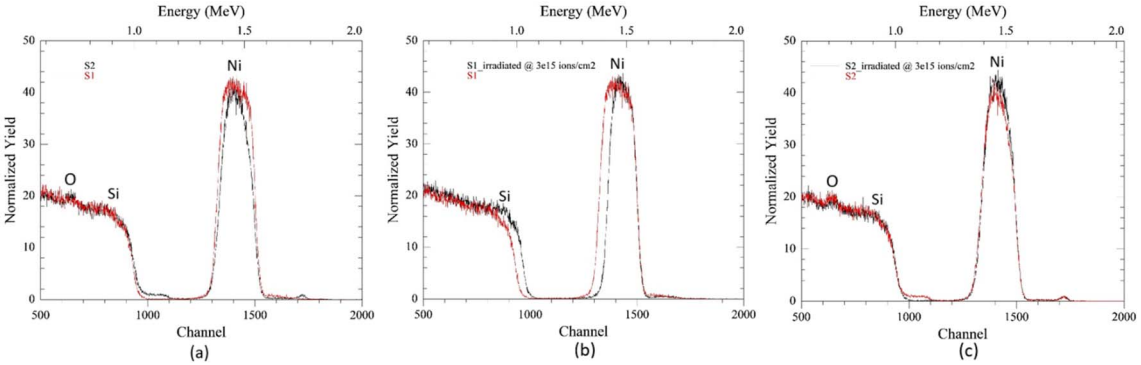

Fig. 6 Comparative RBS spectrum for bilayer sample (a) as deposited and annealed (b) as deposited and irradiated, (c) annealed and irradiated post annealing.

silicide phases. Also, the merging of Ni/Si signals (overlap of Ni low-energy edge and Si high-energy onset) is more apparent in S2, reflecting silicide formation at the interface. And, with the oxygen peak remaining unchanged in both S1 and S2, it denotes no significant new oxidation during the annealing.

In Fig. 6(b), *i.e.*, the RBS spectra of pristine and irradiated S1 films, the nickel peak in the irradiated set becomes narrow and the silicon plateau becomes extended. Reduction in the area under the curve of nickel simply implies that they're in the interface or the mixed Ni/Si region, are diffused or possibly even sputtered![82–84] Si peak becoming broader and shifting towards the higher channel number could imply that the silicon atoms are exposed more than in the case of S1 or are now closer to the surface. Thus, due to the irradiation by negative carbon ions, the distinct Ni becomes narrower (reduced width), Si appears closer to the surface, probably due to reduced Ni shielding, and the interface of nickel and silicon becomes compositionally graded, due to the silicide formation.

Finally, the RBS spectra of pristine and irradiated S2 samples shown in Fig. 6(c) show the disappearance of the intermixed layer at the interface due to irradiation. This is consistent with the GIXRD results of Fig. 3. Irradiation is known not to always enhance mixing, but in some cases, phase dissolution could also happen.[85,86] This is possible when the irradiation energy is sufficient to redistribute atoms of the phase (phase dissolution) in the matrix either ballistically or *via* defects. So, a slight enhanced peak in the nickel could indicate Ni atoms moving back to the surface, or the system might go under relaxation from a mixed silicide state (multiple orientation) into distinct or lowered variation of the phases.

Thus, to conclude, RBS analysis was duly done to investigate the interfacial behavior of Ni(100 nm)/Si(100 nm) bilayers under thermal annealing and carbon ion irradiation. The as-deposited bilayer exhibited a sharp Ni peak and a well-defined Ni–Si interface. Upon annealing at 500 °C for 1 hour, the Ni peak broadened and the Si signal became more graded, indicating interdiffusion and potential formation of nickel silicide. Irradiation of the as-deposited sample led to interface broadening and thinning of the Ni layer, consistent with ion-beam-induced mixing. In contrast, irradiation of the pre-annealed sample resulted in a slight increase and sharpening of the Ni peak, along with a reduced intermixing zone. This suggests a radiation-driven resegregation or interface-sharpening effect, likely influenced by the initial silicide phase stability and preferential atomic displacements under irradiation.

These results highlight the contrasting roles of thermal and irradiation processes in controlling the Ni/Si interface, with implications for controlled silicide formation and interface engineering in thin film systems.

3.3 High resolution transmission electron microscopy (HRTEM)

Electron microscopy is used for its capability to attain a diffraction pattern, which, on analysis, gives in-depth information about the structural avenues of the crystal lattice in a thin film. HRTEM is used to perform a high-definition structural analysis of thin films. Selected Area Electron Diffraction (SAED) uses a selective area or limited area diffraction pattern to get overall information about the crystal planes in the specimen.

Sample preparation for HRTEM measurements of thin films is a significant, intricate, and delicate process requiring meticulous effort. However, among many other methods of sample preparation, we here used the sonication method, where the thin film is sonicated in the IP for ten minutes, which was then drop-cast onto the 300 mesh TEM grid for the analysis.

Fig. 7 shows the SAED patterns for (a) pristine and (b) irradiated S2 samples. The concentric rings with bright spots in Fig. 7(a) are indicative of the fact that the sample contains a polycrystalline structure, which can also be seen in the XRD diffractogram pattern in Fig. 3. Fig. 7(c). The diffused concentric rings for the irradiated samples manifest reduced crystallinity due to ion irradiation, which is in agreement with the GIXRD results of Fig. 3. Reduction in the crystallinity suggests possible damage induced upon the silicide phase or the formation of a disordered Ni–Si structure. The adverse effect of low-energy irradiation of a given fluence is justified from the GIXRD and SAED patterns. Thus, we can safely say that the amorphization of the phases that appeared in the annealed samples has taken place as they were subjected to the irradiation. Also, the

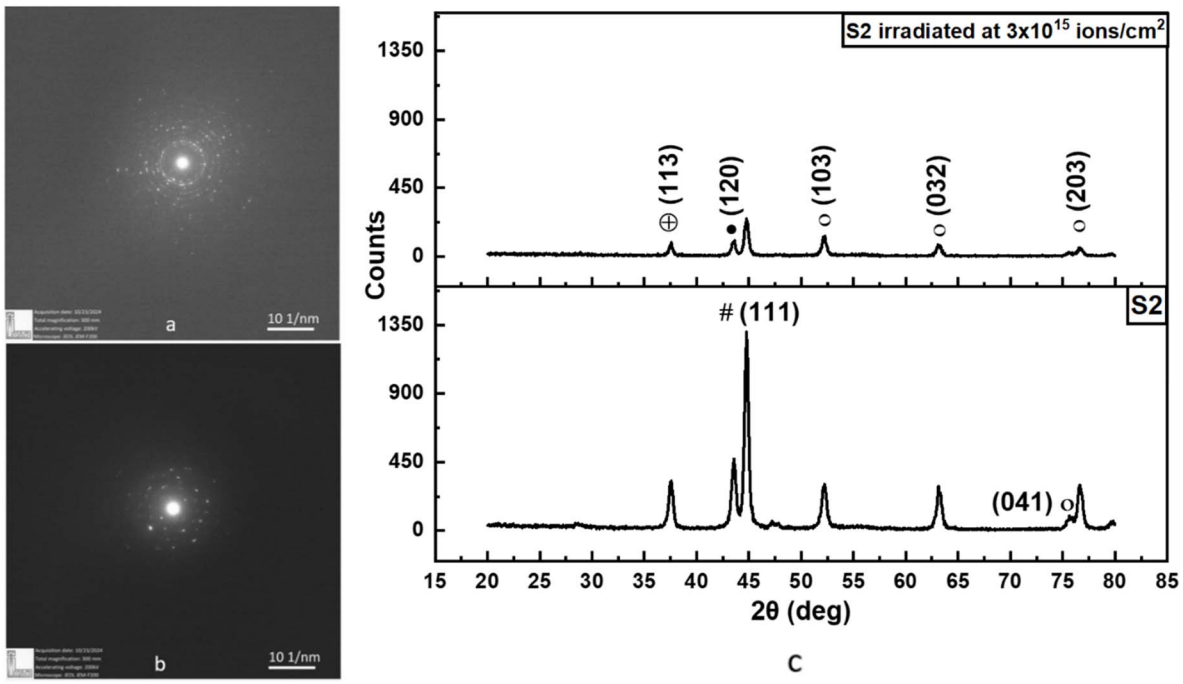

Fig. 7 SAED pattern for (a) annealed sample, (b) irradiated with 3×10^{15} ions per cm^2 post annealing sample, (c) diffractogram comparison of annealed sample and irradiated post annealing sample.

irradiation is seen to cause lattice distortion, reducing the long-range crystallinity. Thus, carbon ion irradiation likely induces Ni–Si interfacial defects, reducing the integrity of the silicide phases.

The high-resolution images obtained from TEM are utilized to identify the crystalline structure and its transformation after irradiation. The HRTEM images in Fig. 8(i) and (ii) depict the annealed bilayer samples and those subjected to irradiation at a fluence of 3×10^{15} ions per cm^2 post-annealing, respectively. ImageJ software was used to analyse these images and determine the lattice parameter (d-spacing).

Fig. 8(i) presents distinct lattice planes corresponding to crystallites formed during annealing. Bragg's equation is used to calculate the d-spacing, keeping the order $n = 1$. Measurement of the d-spacing reveals that the fringes in Fig. 8(i) correspond to (a) Ni_2Si (120), (b & c) NiSi (103) with lattice parameter d equivalent to 0.202 nm and 0.174 correspondingly. Similarly, Fig. 8(ii) presents distinct lattice planes

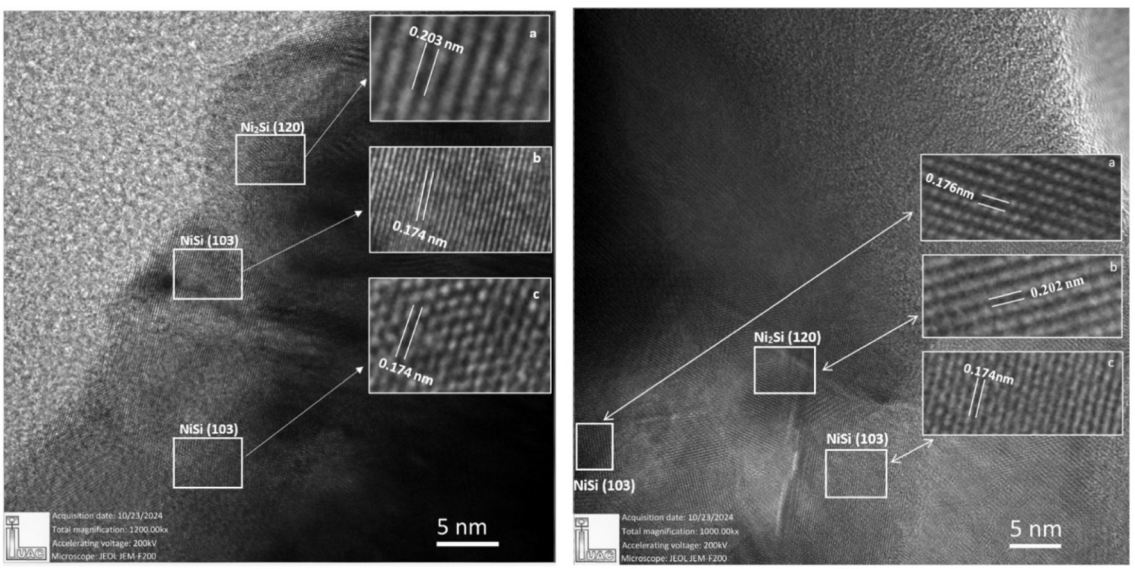

Fig. 8 HRTEM image of (i) annealed bilayer sample, (ii) irradiated at 3×10^{15} ions per cm^2 post annealing sample.

corresponding to crystallites present during irradiation post-annealing. In Fig. 8(ii), the calculated *d* spacing corresponds to (a & c) to NiSi (103) plane and (b) to Ni_2Si(120) plane.

The presence of these phases in both the annealed and post-irradiation samples indicates that the crystallinity remains largely unaffected; however, the number of formed planes decreases significantly after irradiation. This reduction is further supported by the SAED and GIXRD patterns.

4. Conclusion

In conclusion, this experimental study investigates the influence of low-energy, 120 keV negative ion (carbon) beam irradiation on nickel-silicon bilayer thin films deposited *via* magnetron sputtering. The study is further complemented by a comparative analysis with samples that underwent irradiation post-thermal annealing, which is carried out in a tubular furnace at 500 °C under an argon atmosphere. The annealing process was found to play a pivotal role in initiating phase formation within the nickel–silicon system. Several nickel silicide phases were observed to form with high crystallinity, in various orientations, leading to a polycrystalline structure. This polycrystalline nature was distinctly confirmed through the characteristic concentric circle patterns in Selected Area Electron Diffraction (SAED) images, which underscore the diverse grain orientations in the system.

The analysis, conducted using GIXRD and TEM, revealed significant effects of irradiation on the crystallinity of the phases. Specifically, the irradiation disrupted the integrity of the crystalline structure, causing notable damage and inducing alterations in the number of crystallites of silicide phases. The decrease in the intensity of the peaks with increased fluence implies that the growth in the number of crystalline planes is effectively hampered along with the crystallite size; in one of the cases, we observed a reduction in the polycrystallinity but growth in crystallite size (see Fig. 3 and Table 4). The results were strikingly different when the samples were irradiated without any annealing (see Fig. 2). There were no new phases formed; however, the crystallinity is seen to increase as the fluence of the beam increases. These findings underscore the susceptibility of the nickel–silicon system to ion beam-induced structural alterations, highlighting the contrasting outcomes of thermal annealing and ion beam irradiation on phase stability and crystallinity.

RBS analysis confirms nickel–silicon interdiffusion during annealing, forming various nickel silicide phases. Oxygen contamination affects silicide kinetics. Post-irradiation, altered silicide formation suggests phase amorphization or damage. The study highlights how thermal processing and ion irradiation influence film composition, requiring precise control for desired material properties.

HRTEM and SAED analyses reveal structural changes in Ni–Si bilayer films after annealing at 500 °C and subsequent irradiation at a fluence of 3×10^{15} ions per cm^2. SAED shows sharp diffraction spots in annealed samples, which become diffused post-irradiation, indicating lattice distortion and reduced crystallinity. HRTEM images identify lattice planes corresponding to Ni_2Si and NiSi phases, with fewer formed planes post-irradiation. The *d*-spacing analysis using Bragg's equation, further supports these findings. Overall, irradiation disrupts crystallinity, reduces phase integrity, and induces structural disorder, confirming the adverse effects of low-energy carbon ion irradiation on the silicide phases. These findings offer a comprehensive understanding of dose-dependent defect recovery mechanisms and highlight the critical role of crystallographic orientation in influencing defect dynamics. By employing *in situ* characterization techniques under controlled and varying irradiation conditions, this study elucidates the complex interplay between defect formation and recovery processes. Such insights are instrumental for guiding the design and optimization of future advanced materials and devices, particularly those that require precise control over defect-driven phase recovery to achieve enhanced performance and reliability.

Author contributions

Khushboo Shah: writing – review & editing, writing – original draft, investigation, formal analysis, data curation, conceptualization. Ratnesh Pandey: writing – review & editing, visualization, supervision. Santosh Dubey: writing – review & editing, writing – original draft, visualization, supervision, resources, project administration, methodology, investigation, funding acquisition, formal analysis, data curation, conceptualization. Gurupada Maity: writing – review & editing. Mukul Gupta: sample preparation instrumental support. Devirani Devi: low energy (NIBF) experimental facilitation. Sunil Ojha: Rutherford backscattering facilitation.

Conflicts of interest

The authors declare that they have no known competing financial interests or personal relationships that could have appeared to influence the work reported in this paper.

Data availability

In the submitted manuscript, all the figures and tables were generated from our experiments. The data will be provided to the journal whenever it is needed.

Acknowledgements

Khushboo Shah and Santosh Dubey gratefully acknowledge the UGC-DAE Consortium for Scientific Research (CSR), Indore, for providing the necessary facilities at the Sputtering Laboratory for thin film deposition. Sincere thanks is extended to the Pelletron group, Inter University Accelerator Centre (IUAC), New Delhi for access to the Negative Ion Beam Facility (NIBF) for ion irradiation experiments, to the Target Laboratory, IUAC for facilitating the annealing process, TEM Lab for providing expertise in curating TEM samples. Special appreciation and gratefulness to G. Umapathy, Scientist D, IUAC for his guidance and constant support for RBS characterization and data

analysis. We would also wish to express our gratitude to UGC-DAE CSR, Indore for financial support under the project CRS/2021-22/01/412, dated 30-03-2022, and support received from IUAC project with BTR No. 66308. Last but not the least, grateful to R&D, UPES, Dehradun for Fellowship support.

References

1 K. Yamamoto, T. Nakamura, K. Fujimoto, R. Tamura and K. Nishio, Preparation of NiSi2 and application to thermoelectric silicide elements used as electrodes, *MRS Adv.*, 2018, **3**, 1361–1365.
2 H. J. Geipel, N. Hsieh, M. H. Ishaq, C. W. Koburger and F. R. White, Composite Silicide Gate Electrodes-Interconnections for VLSI Device Technologies, *IEEE J. Solid-State Circuits*, 1980, **15**, 482–489.
3 Y. Su, et al., Ultrafine molybdenum silicide nanoparticles as efficient hydrogen evolution electrocatalyst in acidic medium, *Int. J. Hydrogen Energy*, 2022, **47**, 28924–28931.
4 V. S. Poddar, Eco-friendly transition metal silicide for high temperature thermoelectricity, *J. Mater. Sci.: Mater. Electron.*, 2023, **34**, 2067.
5 A. Alberti, F. La Via, M. G. Grimaldi and S. Ravesi, Cobalt silicide thermal stability: from blanket thin film to submicrometer lines, *Solid-State Electron.*, 1999, **43**, 1039–1044.
6 L. J. Chen, Metal silicides: An integral part of microelectronics, *JOM*, 2005, **57**, 24–30.
7 P. L. Tam, Y. Cao, U. Jelvestam and L. Nyborg, Corrosion properties of thermally annealed and co-sputtered nickel silicide thin films, *Surf. Coat. Technol.*, 2011, **206**, 1160–1167.
8 Z. Ye, et al., A promising high-temperature thermal protection performance of silicide-based ceramic coating based on multi-particles/multilayer synergistic design strategy, *Chem. Eng. J.*, 2024, **496**, 153556.
9 S. Knittel, S. Mathieu, L. Portebois, S. Drawin and M. Vilasi, Development of silicide coatings to ensure the protection of Nb and silicide composites against high temperature oxidation, *Surf. Coat. Technol.*, 2013, **235**, 401–406.
10 M. P. Lepselter, A. T. Fiory and N. M. Ravindra, Platinum and rhodium silicide-germanide optoelectronics, *J. Electron. Mater.*, 2008, **37**, 403–416.
11 Y. L. Chueh, L. J. Chou, S. L. Cheng, J. H. He, W. W. Wu and L. J. Chen, Synthesis of taperlike Si nanowires with strong field emission, *Appl. Phys. Lett.*, 2005, **86**(13), 133112.
12 B. Imbert, et al., Impact of surface preparation on nickel-platinum alloy silicide phase formation, *Microelectron. Eng.*, 2007, **84**, 2523–2527.
13 A. Mondon, M. N. Jawaid, J. Bartsch, M. Glatthaar and S. W. Glunz, Microstructure analysis of the interface situation and adhesion of thermally formed nickel silicide for plated nickel–copper contacts on silicon solar cells, *Sol. Energy Mater. Sol. Cells*, 2013, **117**, 209–213.
14 Z. Hussain, V. R. Reddy and S. Dhar, Role of interfacial nickel silicides in shaping magnetic anisotropy in nickel films grown on Silicon substrates, *J. Magn. Magn. Mater.*, 2023, **566**, 170256.
15 A. Mondon, et al., Nanoscale investigation of the interface situation of plated nickel and thermally formed nickel silicide for silicon solar cell metallization, *Appl. Surf. Sci.*, 2014, **323**, 31–39.
16 S. Ramamurthy, et al., Nickel silicides in semiconductor processing: thermal budget considerations, *Mater. Sci. Eng., B*, 2004, **114–115**, 46–50.
17 X. Guo, et al., Study of nickel silicide formation on Si(1 1 0) substrate, *Appl. Surf. Sci.*, 2011, **257**, 10571–10575.
18 V. Lapitskaya, et al., Microstructure and Properties of Thin-Film Submicrostructures Obtained by Rapid Thermal Treatment of Nickel Films on Silicon, *Surfaces*, 2024, **7**, 196–207.
19 A. P. Peter, et al., Phase Formation and Morphology of Nickel Silicide Thin Films Synthesized by Catalyzed Chemical Vapor Reaction of Nickel with Silane, *Chem. Mater.*, 2015, **27**, 245–254.
20 T. Shimozaki, T. Narishige, Y. Wakamatsu and M. Onishi, Reactive Diffusion in a Ni-Si Bulk Diffusion couple, *Mater. Trans.*, 1993, **35**, 868–872.
21 J. H. Liang and D. S. Chao, Formation of tungsten silicide films by ion beam synthesis, *Surf. Coat. Technol.*, 2001, **140**, 116–121.
22 G. Maity, et al., Growth of low resistive nickel mono-silicide phase under low energy Si ion irradiation at room temperature, *Thin Solid Films*, 2021, **733**, 138826.
23 L. S. Wielur, C. Lien, B. X. Liu and M. Nicolet, Improvement of thermally formed nickel silicide by ion irradiation, *J. Vac. Sci. Technol.*, 1982, **20**(2), 182–185.
24 N. Banu, B. Satpati, A. Bhukta and B. N. Dev, Nanoscale η-NiSi formation via ion irradiation of Si/Ni/Si, *J. Appl. Phys.*, 2017, **121**, 045302.
25 R. Ayache, Study of nickel silicide formed by ion beam mixing, *Int. J. Thin Film Sci. Technol.*, 2019, **8**, 37–41.
26 N. Boussaa, A. Guittoum and S. Tobbeche, Formation of Ni2Si silicide in Ni/Si bilayers by ion beam mixing, *Vacuum*, 2005, **77**, 125–130.
27 F. F. Zhao, et al., Thermal stability study of NiSi and NiSi2 thin films, *Microelectron. Eng.*, 2004, **71**, 104–111.
28 G. Utlu, N. Artunç, S. Budak and S. Tari, Structural and electrical characterization of the nickel silicide films formed at 850°C by rapid thermal annealing of the Ni/Si(100) films, *Appl. Surf. Sci.*, 2010, **256**, 5069–5075.
29 M. Bhaskaran, et al., Microstructural investigation of nickel silicide thin films and the silicide-silicon interface using transmission electron microscopy, *Micron*, 2009, **40**, 11–14.
30 C. Perrin, et al., Nickel silicides and germanides: Phases formation, kinetics and thermal expansion, *Mater. Sci. Eng., B*, 2008, **154–155**, 163–167.
31 Y. Setiawan, P. S. Lee, K. L. Pey, X. C. Wang, G. C. Lim and F. L. Chow, Nickel silicide formation using multiple-pulsed laser annealing, *J. Appl. Phys.*, 2007, **101**(3), 034307.
32 Y. Shilyaeva, et al., Thermal and kinetic analyses of silicide formation at nanostructured Si/Ni interface, *J. Therm. Anal. Calorim.*, 2019, **138**, 2339–2345.
33 K. De Keyser, C. Van Bockstael, R. L. Van Meirhaeghe, C. Detavernier, E. Verleysen, H. Bender, W. Vandervorst,

J. Jordan-Sweet and C. Lavoie, Phase formation and thermal stability of ultrathin nickel-silicides on Si(100), *Appl. Phys. Lett.*, 2010, **96**(17), 173503.
34 H. Brahmi, S. Ravipati, M. Yarali, S. Shervin, W. Wang, J. H. Ryou and A. Mavrokefalos, Electrical and optical properties of sub-10 nm nickel silicide films for silicon solar cells, *J. Phys. D: Appl. Phys.*, 2017, **50**(3), 035102.
35 J. P. Lu, et al., A novel nickel SALICIDE process technology for CMOS devices with sub-40 nm physical gate length, in *Technical Digest - International Electron Devices Meeting*, 2002, pp. 371–374, DOI: **10.1109/iedm.2002.1175855**.
36 P. J. Kelly and R. D. Arnell, Magnetron sputtering: a review of recent developments and applications, *Vacuum*, 2000, **56**, 159–172.
37 A. Jain, S. P. Ong, G. Hautier, W. Chen, W. D. Richards, S. Dacek, S. Cholia, D. Gunter, D. Skinner, G. Ceder and K. A. Persson, Commentary: the materials project: a materials genome approach to accelerating materials innovation, *APL Mater.*, 2013, **1**(1), 011002.
38 U. Holzwarth and N. Gibson, The Scherrer equation versus the "Debye-Scherrer equation.", *Nat. Nanotechnol.*, 2011, **6**, 534.
39 S. A. Hassanzadeh-Tabrizi, Precise calculation of crystallite size of nanomaterials: a review, *J. Alloys Compd.*, 2023, **968**, 171914.
40 M. S. Bashar, et al., Effect of rapid thermal annealing on structural and optical properties of ZnS thin films fabricated by RF magnetron sputtering technique, *J. Theor. Appl. Phys.*, 2020, **14**, 53–63.
41 M. M. Kareem, Z. T. Khodair and F. Y. Mohammed, Effect of annealing temperature on structural, morphological and optical properties of ZnO nanorod thin films prepared by hydrothermal method, *J. Ovonic Res.*, 2020, **16**(1), 53–61.
42 E. G. Colgan, M. Mäenpää, M. Finetti and M.-A. Nicolet, Electrical characteristics of thin Ni2Si, NiSi, and NiSi2 layers grown on silicon, *J. Electron. Mater.*, 1983, **12**, 413–422.
43 A. Noya and M. Takeyama, Low-temperature Formation of $NiSi_2$ Phase in Ni/Si System, *IEEJ Trans. Electron. Inf. Syst.*, 2015, **135**, 723–727.
44 I. Blum, A. Portavoce, L. Chow, D. Mangelinck, K. Hoummada, G. Tellouche and V. Carron, B diffusion in implanted Ni_2Si and NiSi layers, *Appl. Phys. Lett.*, 2010, **96**(5), 054102.
45 J. C. Liu and J. W. Mayer, Ion Irradiation Induced Grain Growth in Metal Thin Films, *MRS Proc.*, 1988, **100**, 357.
46 D. E. Alexander and G. S. Was, Thermal-spike treatment of ion-induced grain growth: Theory and experimental comparison, *Phys. Rev. B: Condens. Matter Mater. Phys.*, 1993, **47**, 2983–2994.
47 H. Jensen, et al., Determination of size distributions in nanosized powders by TEM, XRD, and SAXS, *J. Exp. Nanosci.*, 2006, **1**, 355–373.
48 M. Seita, A. Reiser and R. Spolenak, Ion-induced grain growth and texturing in refractory thin films—a low temperature process, *Appl. Phys. Lett.*, 2012, **101**(25), 251905.
49 M. Meier, *Kinetics of grain growth*, 2004.
50 K. H. Chae, et al., The Effect of Thermal Spike on the Ion Irradiation Induced Grain Growth, *MRS Proc.*, 1991, **235**, 565.
51 P. S. Singh, D. Chen, L. Shao, Y. N. Picard and M. P. de Boer, Grain growth stagnation and texture development in an irradiated thermally stabilized nanocrystalline alloy, *J. Appl. Phys.*, 2019, **126**(17), 175901.
52 W. S. Cunningham, K. Hattar, Y. Zhu, D. J. Edwards and J. R. Trelewicz, Suppressing irradiation induced grain growth and defect accumulation in nanocrystalline tungsten through grain boundary doping, *Acta Mater.*, 2021, **206**, 116629.
53 E. J. Mittemeijer, Recovery, Recrystallization and Grain Growth, in *Fundamentals of Materials Science*, Springer Berlin Heidelberg, Berlin, Heidelberg, 2010, pp. 463–496, DOI: **10.1007/978-3-642-10500-5_10**.
54 C. J. Ulmer, W.-Y. Chen, D. E. Wolfe and A. T. Motta, In-situ ion irradiation induced grain growth in nanocrystalline ceria, *J. Nucl. Mater.*, 2021, **545**, 152688.
55 W. J. Weber, Models and mechanisms of irradiation-induced amorphization in ceramics, *Nucl. Instrum. Methods Phys. Res., Sect. B*, 2000, **166–167**, 98–106.
56 L. Wan, L. Chen and Z. Li, Ab initio calculations of interaction between Ni and Si in α-Fe, *J. Nucl. Sci. Technol.*, 2021, **58**, 201–206.
57 A. Kumar Ojha, Density, Hardness, and Melting Points: Key Physical Properties of Binary Crystals, *Int. J. Eng. Sci. Res.*, 2021, **9**(12), 46–59.
58 P. Y. K. R. Brian Flinn, *Fundamentals of Materials Science: Crystal Structures and Properties*, 2006, **https://courses.washington.edu/mse170/powerpoint/Adjorlolo/Chapter_03-12.pdf**.
59 A. Michelmore, *Introduction to Materials*, **https://lo.unisa.edu.au/pluginfile.php/710132/mod_folder/content/0/2ACrystalStructure%282.4MB%29.pdf**.
60 P. H. Chen, et al., Investigation pre-amorphization implantation on nickel silicide formation, in *IEEE International Interconnect Technology Conference*, IEEE, 2014, pp. 249–252, DOI: **10.1109/IITC.2014.6831887**.
61 G. Maity, S. Ojha, G. R. Umapathy, S. P. Patel, A. E. Azab, K. Pandey and S. Dubey, Growth of low resistive nickel mono-silicide phase under low energy Si ion irradiation at room temperature, *Thin Solid Films*, 2021, **733**, 138826.
62 S. J. Zinkle and G. S. Was, Materials challenges in nuclear energy, *Acta Mater.*, 2013, **61**, 735–758.
63 S. Z. Han, et al., Reliable and cost effective design of intermetallic Ni2Si nanowires and direct characterization of its mechanical properties, *Sci. Rep.*, 2015, **5**, 15050.
64 E.-Ha Kim, et al., Ni& gt;inf& lt;2& gt;/inf& lt;Si and NiSi Formation by Low Temperature Soak and Spike RTPs, in *2005 13th International Conference on Advanced Thermal Processing of Semiconductors*, IEEE, 2015, pp. 177–181, DOI: **10.1109/RTP.2005.1613706**.
65 L. Kestens, J. J. Jonas, P. Van Houtte and E. Aernoudt, Orientation selective recrystallization of nonoriented electrical steels, *Metall. Mater. Trans. A*, 1996, **27**, 2347–2358.
66 D. Bowden, J. Ward, S. Middleburgh, S. de Moraes Shubeita, E. Zapata-Solvas, T. Lapauw, J. Vleugels, K. Lambrinou,

W. E. Lee, M. Preuss and P. Frankel, The stability of irradiation-induced defects in Zr3AlC2, Nb4AlC3 and (Zr0.5,Ti0.5)3AlC2 MAX phase-based ceramics, *Acta Mater.*, 2020, **183**, 24–35.

67 W. J. Weber and F. Gao, Irradiation-induced defect clustering and amorphization in silicon carbide, *J. Mater. Res.*, 2010, **25**, 2349–2353.

68 A. L. Kozlovskiy and M. V. Zdorovets, Study of the radiation disordering mechanisms of AlN ceramic structure as a result of helium swelling, *J. Mater. Sci.: Mater. Electron.*, 2021, **32**, 21658–21669.

69 P. Rudolph, Fundamentals and engineering of defects, *Prog. Cryst. Growth Charact. Mater.*, 2016, **62**, 89–110.

70 S. Bist, P. Kalita, S. Shah, N. Singh, R. Gupta, I. Sulania, U. B. Singh, A. K. Chawla, A. Mishra, R. K. Pandey and D. K. Avasthi, Swift heavy ion irradiation effects on tungsten carbide films, *J. Alloys Compd.*, 2024, **976**, 173201.

71 T. de Riese, et al., *Influence of Initial Preferred Orientations on Strain Localisation and Fold Patterns in Non-linear Viscous Anisotropic Materials*, 2020, DOI: **10.5194/egusphere-egu2020-13160**.

72 W. Wu, Y. Nishihara and N. Tsujino, Crystallographic Preferred Orientation of Phase D at High Pressure and Temperature: Implications for Seismic Anisotropy in the Mid-Mantle, *J. Geophys. Res.: Solid Earth*, 2024, **129**, 029734.

73 T. Koyanagi, D. J. Sprouster, L. L. Snead and Y. Katoh, X-ray characterization of anisotropic defect formation in SiC under irradiation with applied stress, *Scr. Mater.*, 2021, **197**, 113785.

74 M. Vashista and S. Paul, Correlation between full width at half maximum (FWHM) of XRD peak with residual stress on ground surfaces, *Philos. Mag.*, 2012, **92**, 1–11.

75 K. Kriti, et al., Influence of defect structure on colour tunability and magneto optical behaviour of WO3 nanoforms, *RSC Adv.*, 2019, **9**, 20536–20548.

76 A. Banerjee, K. V. L. V. Narayanachari and S. Raghavan, Effect of in situ stress on grain growth and texture evolution in sputtered YSZ/Si films, *RSC Adv.*, 2017, **7**, 17832–17840.

77 A. D. Stepukhovich and V. M. Umanskii, Kinetics and Mechanism of Three-Body Recombination of Atoms and Radicals, *Russ. Chem. Rev.*, 1969, **38**(8), 590–607.

78 R. Scheer, Activation energy of heterojunction diode currents in the limit of interface recombination, *J. Appl. Phys.*, 2009, **105**(10), 104505.

79 E. Cao, et al., Activation Energy in the Electron Transfer Process and Water Oxidation Intermediate Generation under Plasmon–Nanocavity Strong Coupling, *J. Phys. Chem. C*, 2025, **129**, 1590–1597.

80 N. T. Chahrazed Dridi, Effects of Carrier Mobility and defects on the Recombination Characteristic of P3HT: Graphene Bulk Heterojunction Solar Cell, *Int. J. Sci. Res. Eng. Technol.*, 2020, **16**, 40–44.

81 A. B. Alwany, G. M. Youssef, E. E. Saleh, O. M. Samir, M. A. Algradee and A. Alnehia, Structural, optical and radiation shielding properties of ZnS nanoparticles QDs, *Optik*, 2022, **260**, 169124.

82 K. Kinoshita, R. Imaizumi, K. Nakajima, M. Suzuki and K. Kimura, Formation of iron silicide on Si(001) studied by high resolution Rutherford backscattering spectroscopy, *Thin Solid Films*, 2004, **461**, 131–135.

83 D. ~J. Coe and E. ~H. Rhoderick, Silicide formation in Ni-Si Schottky barrier diodes, *J. Phys. D Appl. Phys.*, 1976, **9**, 965–972.

84 A. K. N. Kumar, S. Jayakumar, M. D. Kannan, S. Rajagopalan, A. K. Balamurugan, A. K. Tyagi, S. Kumar, G. L. N. Reddy, J. V. Ramana and V. S. Raju, Surface and interface reactions of sputtered TiNi/Si thin films, *J. Appl. Phys.*, 2009, **105**(6), 063517.

85 C.-C. Tin, S. Mendis, M. T. Tin, T. Isaacs-Smith and J. R. Williams, A new approach in impurity doping of 4H-SiC using silicidation, *J. Appl. Phys.*, 2013, **114**(24), 244502.

86 N. Boussaa, A. Guittoum and S. Tobbeche, Formation of Ni2Si suicide in Ni/Si bilayers by ion beam mixing, *Vacuum*, 2005, **77**, 125–130.